Applied Physics Express

LETTER • **OPEN ACCESS**

Accelerated ferroelectric phase transformation in HfO_2/ZrO_2 nanolaminates

OPEN ACCESS

Applied Physics Express 14, 051006 (2021) LETTER

https://doi.org/10.35848/1882-0786/abfa75

Accelerated ferroelectric phase transformation in HfO_2/ZrO_2 nanolaminates

Shinji Migita[1*], Hiroyuki Ota[1], Shutaro Asanuma[1], Yukinori Morita[1], and Akira Toriumi[2]

[1]National Institute of Advanced Industrial Science and Technology, 1-1-1 Umezono, Tsukuba, Ibaraki 305-8568, Japan
[2]Department of Materials Engineering, The University of Tokyo, 7-3-1 Hongo, Bunkyo, Tokyo 113-8656, Japan

*E-mail: s-migita@aist.go.jp

Received March 20, 2021; revised April 12, 2021; accepted April 21, 2021; published online May 4, 2021

Ferroelectric phase transformation was compared between the $Hf_{0.5}Zr_{0.5}O_2$ solid solution films and the HfO_2/ZrO_2 nanolaminate films, prepared by sputter deposition without heat treatment and crystallized by following cap annealing. Physical analyses showed that nanolaminate structures and their interfaces were robust even after high-temperature annealing. Ferroelectricity appeared largely in the nanolaminate films than in the solid solution film, and the best performance was attained in the nanolaminate film with the cycle thickness of monolayer oxide (0.25 nm). Long period annealing cleared that the ferroelectric phase transformation is greatly accelerated in the nanolaminate films than in the solid solution films.

HfO_2 is a polymorphic compound with several crystal structures including cubic, tetragonal, and monoclinic ones. First-principle calculations predicted that the dielectric properties would differ between these crystal structures.[1)] Experiments have demonstrated that the crystallization of cubic HfO_2 films via metal element doping[2,3)] and cap annealing[4)] can drastically change the dielectric constant. The emergence of ferroelectricity was reported in doped HfO_2 thin films,[5,6)] which was attributed to the formation of orthorhombic crystal structure.[5,7)] To stabilize the ferroelectric property in films, many different dopants at optimal concentrations are used.[8–11)] Applying mechanical stresses using substrates[12)] and electrode films[13)] and controlling the oxygen content[14–16)] are also effective. These findings have been combined with calculations to explain the formation mechanism of the orthorhombic crystal structure and the enhancement of ferroelectricity.[17–20)] Managing the heat treatment is crucial in the formation of the orthorhombic structure during the structural transformation between the tetragonal and monoclinic ones.[21–26)]

In particular, the ferroelectric properties of Hf–Zr–O are tolerant to a varying ratio of metal elements; its ideal composition is $Hf_{0.5}Zr_{0.5}O_2$.[11,27,28)] Experimental demonstrations of very fast switching,[29)] high endurance,[30)] and operation under low voltage[31)] have proven the potential of Hf–Zr–O films for memory device applications in large-scale integrated circuits.[32–34)] They have predominantly been prepared through atomic-layer deposition (ALD) and crystallization annealing. Bi-layer,[35)] seed-layer,[36)] and nanolaminate[33,37,38)] deposition techniques have been studied to improve the ferroelectricity of $Hf_{0.5}Zr_{0.5}O_2$ films. The nanolaminate production is a promising approach that cannot be achieved in other doped HfO_2 systems. A 1 nm thick cyclic deposition of HfO_2 and ZrO_2 layers produced superior ferroelectric properties.[37)] Moreover, selecting the starting layer (HfO_2 or ZrO_2) was shown to be critical because the in situ crystallization during ALD influences subsequent electrical performance.[38)]

This study explored the significance of the HfO_2/ZrO_2 nanolaminate structures for the enhancement of ferroelectricity, in comparison with the solid solution $Hf_{0.5}Zr_{0.5}O_2$ films. To avoid in situ crystallization during deposition, we applied the sputter deposition technique without heating the substrate. The thinnest nanolaminate cycle was 0.25 nm, similar with the monolayer oxide thickness in the $Hf_{0.5}Zr_{0.5}O_2$ crystal. Evolution of the ferroelectric phase was traced by long-duration annealing. These investigations enable a better understanding of the mechanisms leading to superior ferroelectric properties, thereby allowing optimized production.

Heavily doped 2 inch Si (100) wafers were used as substrates after removing the native oxides with a HF solution. The complex deposition system consisted of a direct current (DC) chamber and a radio frequency (RF) sputtering chamber. In the DC sputtering chamber, 10 mn thick TaN films were deposited at a rate of 0.042 nm s^{-1} by sputtering the Ta target in a gas mixture of Ar and N_2 and were used as the bottom and top electrodes of the capacitors. HfO_2, ZrO_2, and $Hf_{0.5}Zr_{0.5}O_2$ targets were set in the RF sputtering chamber using three individual sputtering sources equipped with mechanical shutters; the deposition rates were 0.042, 0.019, and 0.040 nm s^{-1}, respectively. The solid solution $Hf_{0.5}Zr_{0.5}O_2$ film was prepared using a $Hf_{0.5}Zr_{0.5}O_2$ target. HfO_2/ZrO_2 nanolaminates were prepared using HfO_2 and ZrO_2 targets, by opening the mechanical shutters alternately by computer control.[28)] The thicknesses produced by the nanolaminate cycles were 0.25, 0.5, 1.0, 1.5, and 2.0 nm. The film thicknesses and metal compositions were verified via TEM, monochromatic ellipsometry, and X-ray photoelectron spectroscopy. The film thicknesses for electrical measurements were adjusted to 12 nm. For example, the 0.25 nm-cycle nanolaminate comprised (0.25 nm HfO_2 + 0.25 nm ZrO_2) × 24 cycles. The sputter-deposited TaN and Hf–Zr–O films were amorphous. After depositing the bottom TaN, Hf–Zr–O, and top TaN films, the wafers were annealed using a quartz furnace in 1 atm N_2. Subsequently, 300 nm-thick aluminum films were deposited on both sides of the wafers as supporting electrodes. Using lithography and dry etching techniques, the top electrode patterns were formed. The capacitor size was 100 μm × 100 μm. Polarization–electric field (P–E) characteristics were measured using a ferroelectric tester (Radiant Technologies Inc., Premier II) at a frequency of 1 kHz. The range of the applied voltage was between −3 and 3 V. This work compared the fresh

properties by limiting the cycle number of an electrical field to be less than 10. Reproducibility was confirmed by the measurements of more than eight capacitors on each wafer.

Previously,[25] we systematically investigated the relationship between the crystal structure and electrical behavior of 10 nm thick $Hf_{0.5}Zr_{0.5}O_2$ films by changing the annealing temperature and time. The amorphous $Hf_{0.5}Zr_{0.5}O_2$ films were prepared by sputtering in a laminate-like deposition manner. As a result, the tetragonal structure was revealed to crystallize first and show anti-ferroelectric-like behavior, subsequently changing to an orthorhombic structure with ferroelectric behavior, and finally to a monoclinic structure with linear dielectric behavior. This phase change was fast when the annealing temperature was high, and the monoclinic phase was the final product obtained after excessive thermal treatment. Based on these results, we discussed the crystal structures by relying on *P*–*E* measurements.

Figure 1 shows the characterization results for the nanolaminate structures after heat treatment. The 2.0 nm cycle HfO_2/ZrO_2 nanolaminates with TaN electrode films were annealed at 600 °C for 10 min. The high-angle annular dark-field scanning TEM image and energy dispersive X-ray spectroscopy mappings of Hf and Zr show that the nanolaminate structure is maintained regularly with flat interfaces [Fig. 1(a)]. Next, the depth profiles of Hf and Zr atoms in HfO_2 (3 nm)/ZrO_2 (5 nm)/HfO_2 (3 nm) structures of the as-deposited and annealed samples were analyzed by high-resolution Rutherford backscattering spectroscopy [Fig. 1(b)]. Although excessive annealing was performed at 800 °C for 10 min in a vacuum, the diffusion and intermixing of metallic elements were negligible. Thus, HfO_2–ZrO_2 interfaces in the nanolaminates are robust even after crystallization annealing. These results concur with the characteristics reported in earlier studies using ALD[33,37,38] and show that sputter deposition is appropriate to produce nanolaminates.

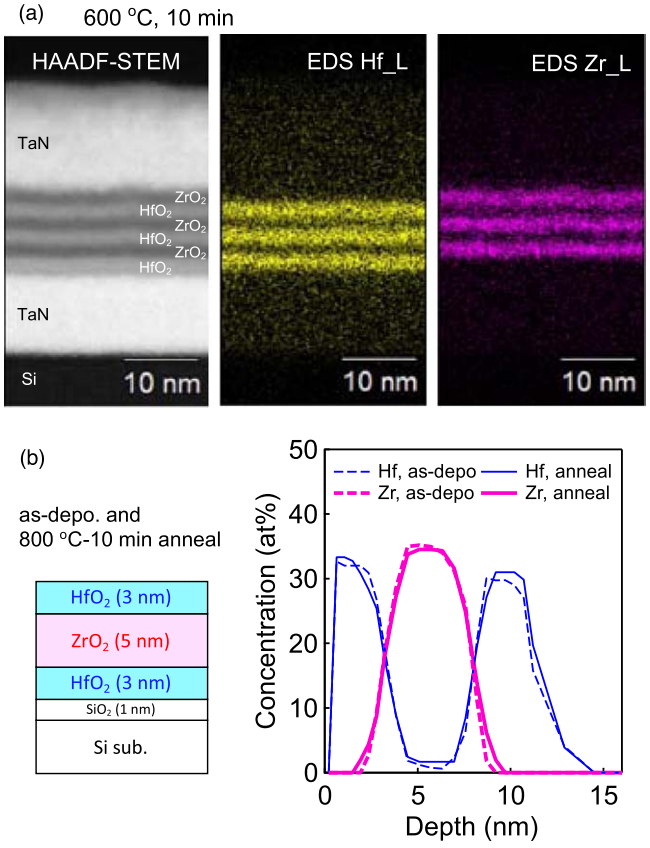

Fig. 1. (Color online) (a) HAADF-STEM and EDS mapping images of 12 nm thick HfO_2/ZrO_2 nanolaminates (2 nm cycle) between two TaN films on a Si substrate, annealed at 600 °C for 10 min in 1 atm N_2. (b) HR-RBS analysis of HfO_2 (3 nm)/ZrO_2 (5 nm)/HfO_2 (3 nm) structures on SiO_2/Si substrates, as-deposited (dashed lines) and annealed at 800 °C for 10 min in vacuum (solid lines).

Figure 2 shows the *P*–*E* characteristics of the 12 nm thick $Hf_{0.5}Zr_{0.5}O_2$ solid solution film and HfO_2/ZrO_2 nanolaminate films annealed at 600 °C for 10 min in 1 atm N_2. The response of the solid solution film is almost linear. The dielectric constant calculated from the slope was 34. This indicates that the solid solution film formed a higher-*k* crystalline film. The anti-ferroelectric-like hysteresis indicates the presence of the tetragonal structure. In contrast, the nanolaminate films have square hysteresis loops caused by ferroelectricity in the orthorhombic structure. Nanolaminate films can induce stronger ferroelectric properties than the solid solution films. Components of pinched hysteresis behaviors are observable in some nanolaminate cases, suggesting the coexistence of the tetragonal and orthorhombic structures and exhibiting the transition from the former to the latter structure.[25]

The correlation between the degree of the ferroelectric phase formation and the thickness of the nanolaminate layers was summarized using remanent polarization (P_r) (Fig. 3). The P_r value of the solid solution film was not measurable, while the P_r values of the nanolaminate films were large. The observation that a thinner layer is more favorable for ferroelectricity is consistent with past nanolaminate studies using ALD,[37,38] and our work further includes the properties of nanolaminate layers down to a thickness of 0.25 nm. This thickness corresponds to the half-unit cell and the monolayer oxide thickness of (001)-oriented HfO_2 and ZrO_2 crystals.[5,7] Although the as-deposited Hf–Zr–O films are amorphous, engineering film deposition at monolayer levels largely contribute to optimize ferroelectric phase formation. In

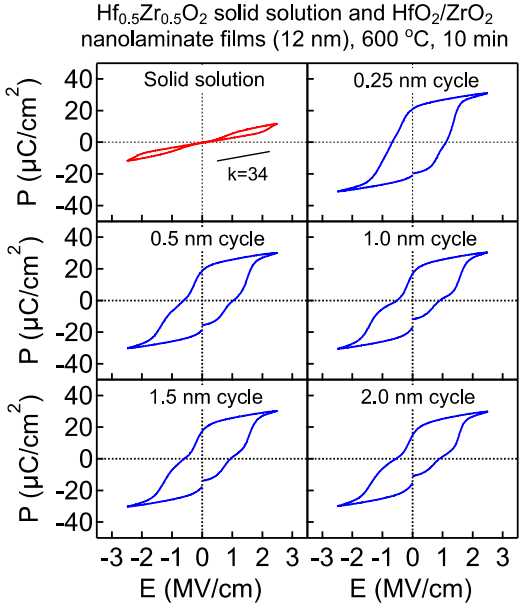

Fig. 2. (Color online) Polarization–electric field (*P*–*E*) characteristics of 12 nm thick $Hf_{0.5}Zr_{0.5}O_2$ solid solution and HfO_2/ZrO_2 nanolaminate films annealed at 600 °C for 10 min.

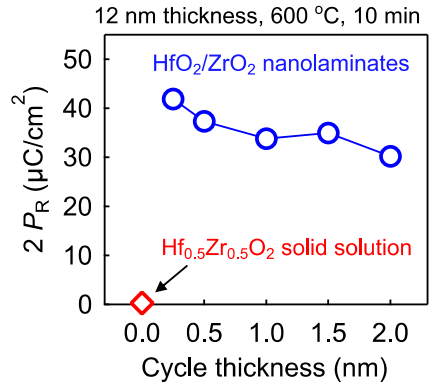

Fig. 3. (Color online) Dependence of remnant polarization, P_r, on the cycle thickness of HfO_2/ZrO_2 nanolaminates. The case of solid solution film is shown for a 0 nm cycle.

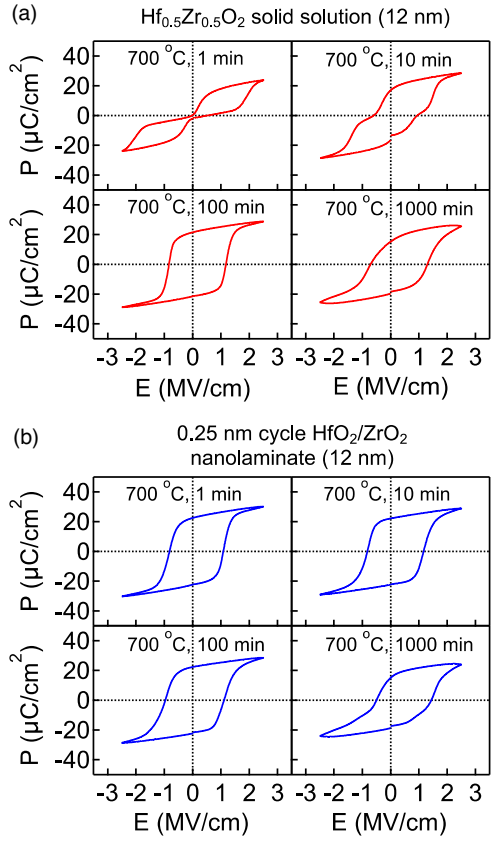

Fig. 4. (Color online) Polarization–electric field (P–E) characteristics of 12 nm thick (a) $Hf_{0.5}Zr_{0.5}O_2$ solid solution films and (b) 0.25 nm cycle HfO_2/ZrO_2 nanolaminate films, annealed at 700 °C for different durations.

general, ALD is known as a technique to prepare oxide films with atomic-scale precision, albeit with two concerns. Firstly, the one-cycle thickness of ALD films does not complete the monolayer because the molecular sizes of ALD precursors are large.[39] Secondly, the crystallization of films is initiated during ALD, even though the deposition temperature is not very high.[37,38] Therefore, taking measures to ensure monolayer coverage and suppress crystallization during deposition is indispensable when employing ALD.

Next the transformation of ferroelectric properties was studied with annealing time. The solid solution and 0.25 nm cycle nanolaminate films prepared by sputter deposition were cap-annealed at 700 °C for 1, 10, 100, and 1000 min in 1 atm N_2. Figure 4(a) shows the P–E characteristics of the solid solution films. The 1 min annealed capacitor demonstrates clear anti-ferroelectric-like behavior, suggesting the formation of the tetragonal structure. Longer annealing times resulted in good ferroelectric properties owing to structural change from tetragonal to orthorhombic. Finally, the ferroelectricity of the 1000 min annealed sample degraded because of the partial transition to the monoclinic structure.[25] The P–E characteristics of the 0.25 nm cycle nanolaminate films [Fig. 4(b)] were different; superior ferroelectric properties were attained, despite annealing for 1 min only. This advantage was maintained for 10 and 100 min annealing but degraded with 1000 min annealing.

Figure 5(a) summarizes the evolution of ferroelectric properties in the solid solution films with different annealing times at 700 °C and in the 0.25 nm cycle nanolaminate films. Both types of films achieve the same maximum P_r values; however, the required annealing times vary. Previous reports showed that nanolaminates contribute to the volume fraction of the ferroelectric phase,[37,38] whereas this work reveals that nanolaminates accelerate the ferroelectric phase transformation. In contrast, the ferroelectric properties were degraded after prolonged heat treatment, irrespective of the film deposition style. Figure 5(b) shows the crystallinity of solid solution and nanolaminate films at their best ferroelectric conditions, measured by in-plane XRD (incident angle is 0.7°). Both films show similar polycrystalline diffraction patters. Thus, nanolaminate structures does not influence on the crystal orientation of the films.

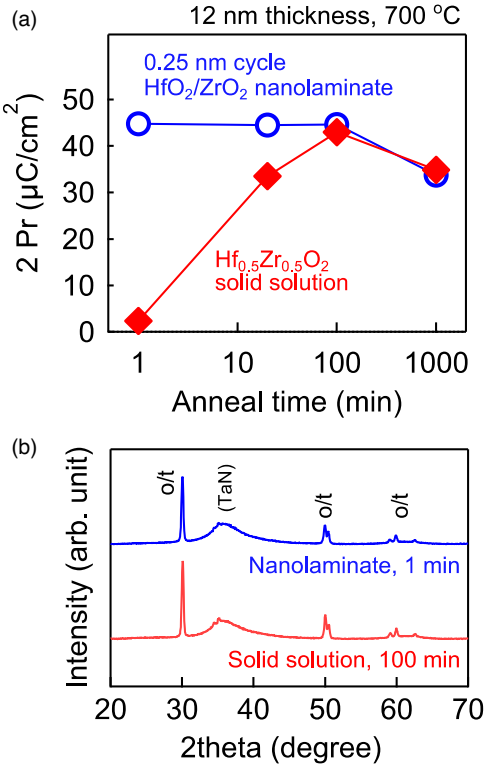

Fig. 5. (Color online) (a) Transition of ferroelectricity (remnant polarization, P_r) in 12 nm thick $Hf_{0.5}Zr_{0.5}O_2$ solid solution films with indicated annealing times and in 0.25 nm cycle HfO_2/ZrO_2 nanolaminate films. (b) IP-XRD patterns of 12 nm thick $Hf_{0.5}Zr_{0.5}O_2$ solid solution film (700 °C for 100 min) and 0.25 nm cycle HfO_2/ZrO_2 nanolaminate films (700 °C for 1 min). The broad amorphous signals come from the TaN films on top of Hf–Zr–O films.

We consider the impact of nanolaminate films as follows. In the structural change from tetragonal to orthorhombic, the oxygen arrangement changes from centrosymmetric to noncentrosymmetric.[5,7] This change might be assisted by the local force in the unit cell of crystal. According to the related free energies of formation, HfO_2 is slightly more stable than ZrO_2.[40] Therefore the Hf–O bond is somewhat stronger than the Zr–O bond, which results in an unbalanced bonding strength between Hf–O and Zr–O. In the solid solution film, the unbalanced bonding does not work effectively because the arrangement of Hf and Zr atoms in the crystal unit cell is random. On the other hand, in the nanolaminate film, the unbalanced bonding strengths are enhanced at the HfO_2 and ZrO_2 interfaces. We believe that this effect might induce the nucleation of orthorhombic structure and accelerate the ferroelectric phase formation.

In summary, ultimately thin nanolaminate films fabricated by the cyclic deposition of HfO_2 and ZrO_2 monolayers demonstrated superior ferroelectric properties after crystallization anneal. During production, it is important to complete the monolayer in each cycle and suppress in situ crystallization during deposition. The benefit of a nanolaminate structure is that it accelerates the phase transformation, which provides a larger process margin for the attainment of metastable ferroelectric phase.

Acknowledgments This work was supported by JST CREST, Grant Number JPMJCR14F2; JST Japan-Taiwan Collaboration Research Program, Grant Number JPMJKB1903; and JSPS KAKENHI, Grant Number 20H2445.

ORCID iDs Yukinori Morita https://orcid.org/0000-0002-2666-6762

1) X. Zhao and D. Vanderbilt, Phys. Rev. B **65**, 233106 (2002).
2) K. Kita, K. Kyuno, and A. Toriumi, Appl. Phys. Lett. **86**, 102906 (2005).
3) K. Tomida, K. Kita, and A. Toriumi, Appl. Phys. Lett. **89**, 142902 (2006).
4) S. Migita, Y. Watanabe, H. Ota, H. Ito, Y. Kamimuta, T. Nabatame, and A. Toriumi, Dig. Tech. Pap.—Symp. VLSI Technol., 2008, p. 152.
5) T. S. Böscke, J. Müller, D. Bräuhaus, U. Schröder, and U. Böttger, Appl. Phys. Lett. **99**, 102903 (2011).
6) J. Müller, T. S. Böscke, D. Bräuhaus, U. Schröder, U. Böttger, J. Sundqvist, P. Kücher, T. Mikolajick, and L. Frey, Appl. Phys. Lett. **99**, 112901 (2011).
7) X. Sang, E. D. Grimley, T. Schenk, U. Schroeder, and J. M. LeBeau, Appl. Phys. Lett. **106**, 162905 (2015).
8) U. Schroeder, E. Yurchuk, J. Müller, D. Martin, T. Schenk, P. Polakowski, C. Adelmann, M. I. Popovici, S. V. Kalinin, and T. Mikolajick, Jpn. J. App. Phys. **53**, 08LE02 (2014).
9) S. Starschich and U. Boettger, J. Mater. Chem. C **5**, 333 (2017).
10) M. H. Park, T. Schenk, C. M. Fancher, E. D. Grimley, C. Zhou, C. Richter, J. M. LeBeau, J. L. Jones, T. Mikolajick, and U. Schroeder, J. Mater. Chem. C **5**, 4677 (2017).
11) L. Xu, T. Nishimura, S. Shibayama, T. Yajima, S. Migita, and A. Toriumi, J. Appl. Phys. **122**, 124104 (2017).
12) T. Shiraishi et al., Appl. Phys. Lett. **108**, 262904 (2016).
13) S. J. Kim et al., Appl. Phys. Lett. **111**, 242901 (2017).
14) T. Nishimura, L. Xu, S. Shibayama, T. Yajima, S. Migita, and A. Toriumi, Jpn. J. Appl. Phys. **55**, 08PB01 (2016).
15) A. Pal, V. K. Narasimhan, S. Weeks, K. Littau, D. Pramanik, and T. Chiang, Appl. Phys. Lett. **110**, 022903 (2017).
16) U. Schroeder, M. Materano, T. Mittmann, P. D. Lomenzo, T. Mikolajick, and A. Toriumi, Jpn. J. Appl. Phys. **58**, SL0801 (2019).
17) S. Clima, D. J. Wouters, C. Adelmann, T. Schenk, U. Schroeder, M. Jurczak, and G. Pourtois, Appl. Phys. Lett. **104**, 092906 (2014).
18) S. E. Reyes-Lillo, K. F. Garrity, and K. M. Rabe, Phys. Rev. B **90**, 140103 (2014).
19) R. Materlik, C. Künneth, and A. Kersch, J. Appl. Phys. **117**, 134109 (2015).
20) R. Batra, T. D. Huan, J. L. Jones, G. Rossetti Jr, and R. Ramprasad, J. Phys. Chem. C **121**, 4139 (2017).
21) T. S. Böscke, S. Teichert, D. Bräuhaus, J. Müller, U. Schröder, U. Böttger, and T. Mikolajick, Appl. Phys. Lett. **99**, 112904 (2011).
22) M. Hoffmann et al., J. Appl. Phys. **118**, 072006 (2015).
23) M. H. Park, C. Chung, T. Schenk, C. Richter, K. Opsomer, C. Detavernier, C. Adelmann, J. L. Jones, T. Mikolajick, and U. Schroeder, Adv. Electron. Mater. **4**, 1800091 (2018).
24) S. Shibayama, T. Nishimura, S. Migita, and A. Toriumi, J. Appl. Phys. **124**, 184101 (2018).
25) S. Migita, H. Ota, K. Shibuya, H. Yamada, A. Sawa, T. Matsukawa, and A. Toriumi, Jpn. J. Appl. Phys. **58**, SBBA07 (2019).
26) M. H. Park, Y. H. Lee, T. Mikolajick, U. Schroeder, and C. S. Hwang, Adv. Electron. Mater. **5**, 1800522 (2019).
27) J. Müller, T. S. Böscke, U. Schröder, S. Mueller, D. Braühaus, U. Böttger, L. Frey, and T. Mikolajick, Nano Lett. **12**, 4318 (2012).
28) S. Migita, H. Ota, H. Yamada, K. Shibuya, A. Sawa, and A. Toriumi, Jpn. J. Appl. Phys. **57**, 04FB01 (2018).
29) M. Si, X. Lyu, P. R. Shrestha, X. Sun, H. Wang, K. P. Cheung, and P. D. Ye, Appl. Phys. Lett. **115**, 072107 (2019).
30) T. Mittmann, F. P. G. Fengler, C. Richter, M. H. Park, T. Mikolajick, and U. Schroeder, Microelectron. Eng. **178**, 48 (2017).
31) S. J. Kim, J. Mohan, H. S. Kim, J. Lee, C. D. Young, L. Colombo, S. R. Summerfelt, T. San, and J. Kim, Appl. Phys. Lett. **113**, 182903 (2018).
32) J. Müller et al., IEEE IEDM, 2013, p. 10.8.1.
33) S. Riedel, P. Polakowski, and J. Müller, AIP Adv. **6**, 095123 (2016).
34) K. Maekawa, T. Yamaguchi, T. Ohara, A. Amo, E. Tsukuda, K. Sonoda, H. Yanagita, M. Inoue, M. Matsuura, and T. Yamashita, IEEE IEDM, 2019, p. 15.4.1.
35) Y. W. Lu, J. Shieh, and F. Y. Tsai, Acta Mater. **115**, 68 (2016).
36) T. Onaya, T. Nabatame, N. Sawamoto, A. Ohi, N. Ikeda, T. Chikyow, and A. Ogura, Appl. Phys. Express **10**, 081501 (2017).
37) S. L. Weeks, A. Pal, V. K. Narasimhan, K. A. Littau, and T. Chiang, ACS Appl. Mater. Interfaces **9**, 13440 (2017).
38) M. H. Park et al., Appl. Phys. Rev. **6**, 041403 (2019).
39) M. Materano, C. Richter, T. Mikolajick, and U. Schroeder, J. Vac. Sci. Technol. A **38**, 022402 (2020).
40) S. Stemmer, J. Vac. Sci. Technol. B **22**, 791 (2004).